Space: Science & Technology
A SCIENCE PARTNER JOURNAL

RESEARCH ARTICLE

A Novel Design and Optimization Method for an Electrodynamic Tether Deployment Mechanism

Yi Yang[1], Keying Yang[1*], Jingrui Zhang[1], Han Cai[1], Chunyang Zhou[1], and Lincheng Li[2,3]

[1]School of Aerospace Engineering, Beijing Institute of Technology, 5th South Zhongguancun Street, Beijing 100081, China. [2]School of Astronautics, Beihang University, 37 Xueyuan Road, Beijing 100091, China. [3]School of Electrical and Electronic Engineering, Nanyang Technological University, 50 Nanyang Avenue, Singapore 639798, Singapore.

*Address correspondence to: yangkeying@bit.edu.cn

Citation: Yang Y, Yang K, Zhang J, Cai H, Zhou C, Li L. A Novel Design and Optimization Method for an Electrodynamic Tether Deployment Mechanism. *Space Sci. Technol.* 2024;4:Article 0147. https://doi.org/10.34133/space.0147

Submitted 10 July 2023
Accepted 10 March 2024
Published 25 April 2024

In the field of active deorbiting technologies, the electrodynamic tether has garnered attention due to its cost-effectiveness, light weight, and low fuel consumption. In this study, to address the low success rate of the deployment mechanisms used in previous in-orbit experiments, a novel deployment mechanism with a size of 2 U and a weight 2.3 kg based on pusher motors is proposed. In order to achieve a smooth tether deployment without rupture and rebound, an optimization method was proposed for springs, and tether within the deployment mechanism. Finally, simulation and ground ejection experiment were conducted with the objective of deploying a 50-m tether. In the experiment, the top plate was ejected with a kinetic energy of 2.3 J, and the tether was successfully unfolded. The experimental results indicate that the device is capable of deploying a tether of at least 50 m, demonstrating the effectiveness of the optimization method.

Introduction

Electrodynamic tether is a highly promising deorbiting tool since it has the following advantages [1–4]. One is that the device's deorbiting effect and control algorithm design is robust to the parameters [5] and attitude [6] of the spacecraft to be deorbited. The other is that the electrodynamic tether device offers better versatility and lower design effort compared to other deorbiting devices [5].

However, the electrodynamic tether device suffers from a high failure rate of deployment [7]. The Tethered Satellite System (TSS-1) project conducted by the National Aeronautics and Space Administration in 1992 experienced a jamming issue after the reel mechanism malfunctioned, resulting in the release of only 250 m of tether [8]. In 2010, the Tether Rocket experiment (T-REX) project carried out by Japan Aerospace Exploration Agency (JASA) achieved a successful release of a tape-like tether measuring 132.6 m. However, it encountered jamming due to excessive resistance [9]. The Konotori Integrated Tether Experiment (KITE) experiment in 2017 encountered a release failure caused by a separation bolt malfunction [5]. In more than a dozen experiments conducted in various countries, nearly half of them failed due to tether deployment failure.

To address the aforementioned issues, this study proposes an electrodynamic tether deployment mechanism based on pusher motors. To decrease the probability of jamming during the tether deployment, it is the key to reduce the release resistance. Additionally, to prevent rupture due to jamming, initial ejection velocity and tether parameters should also be considered. Thus, this paper proposes an optimization method to elaborately design the above parameters and conducts ground ejection experiments to verify the optimization method as well as the functionality of the deployment mechanism.

The remainder of the paper is organized as follows: the "Design of the Deployment Mechanism" section presents the design of the electrodynamic tether deployment mechanism and analyzes its mechanical properties. To avoid jamming and rupture, the "Optimization Method for Electrodynamic Tether Deployment Mechanism" section proposes an optimization method for parts of the deployment mechanism. Through ground ejection experiments, the feasibility of the optimization method and the functionality of the deployment mechanism are verified. Finally, Discussion summarizes the study and provides future directions.

Materials and Methods

Mechanical structure of the deployment mechanism

To solve the problems in the onboard experiments, we propose an innovative electrodynamic tether deployment mechanism as shown in Fig. 1. The deployment mechanism is divided into 14 core parts, while parts 1 to 9 form the locking and unlocking module and parts 10 to 12 constitute the tether storage module.

Workflow of the deployment mechanism

The deployment mechanism works as follows (Fig. 2):

1. Step 1: Safety Unlocking. The push rod motor drives the safety forward until it reaches the limit position, releasing the lock on the pusher movement.

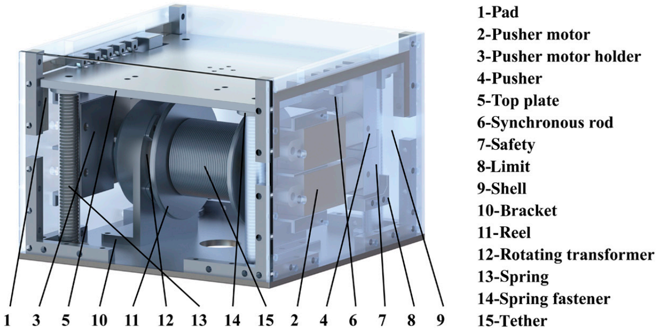

Fig. 1. Model of the deployment mechanism.

Note that except for top plate and synchronous rod, each part of the locking and unlocking module is in pairs to balance the force condition of top plate. They are installed inside the 2 sides of the shell opposite to each other.

2. Step 2: Pusher Translation. The pusher motor drives the pusher forward until the teeth on the upper end of the pusher intersect with the teeth on the top plate, releasing the lock on the top plate and the spring.

In this step, there is a huge friction between the pusher and the top plate due to the force exerted by the spring pressure. To reduce friction and decrease the thrust requirement on the pusher motor, bearings are installed within the teeth of the pusher, converting sliding friction into rolling friction.

3. Step 3: Ejection and Deployment. Once the spring is unlocked, the elastic potential energy of the spring is converted into the kinetic energy of the top plate. The top plate is ejected with a certain initial velocity, simultaneously initiating the deployment of the tether.

Advantages of the deployment mechanism

The deployment mechanism has the following advantages:

1. It is innovative. Orbital experiments of electrodynamic tether have not yet recorded the use of pusher motor for unlocking.
2. It has good synchronicity. By ensuring both mechanical and electronic synchronization, the device exhibits favorable unlocking synchronicity.
3. It has good safety. Compared with firework products, this device is completely driven by electricity and has no vibration when unlocking.
4. It is low cost. Compared with the memory alloy releasing mechanism [10], this mechanism has good reusability, so it can effectively reduce experimental costs when multiple experiments are required for ground testing scenarios.
5. It has light weight and small volume. The final design of the device has a size of 1.4×1.4×1.0 dm = 1.96 U and has a total weight of less than 2.3 kg (excluding tethers). Compared to orbital experiments such as Space Tethered Autonomous Robotic Satellite (STARS) [11] and KITE [5], this mechanism offers advantages in terms of lightweight and compact design, which is more in line with the future development trend of space payloads [12].
6. It has a large capacity of tether. It can accommodate 2 tethers of approximately 250 m in length and 0.4 mm in diameter, which is twice the capacity of STARS satellites [11] of the same volume.

Optimization method and objectives for electrodynamic tether deployment mechanism

The content of the next 3 sub-sections are illustrated in Fig. 3. To achieve a smooth deployment of the conductive tether without rupture and rebound, an optimization approach is proposed in this section. This approach includes optimizing the tether material to prevent rupture. Additionally, it focuses on reducing the risk of jamming by optimizing the tether configuration to decrease ejection resistance. The tether breakage criteria are also introduced as constraints in the configuration optimization problem to prevent rupture. To avoid rebound, careful consideration is given to the design of the ejection initial velocity, which is achieved through spring selection.

Optimization to prevent rupture

To prevent rupture, the tether should be made from materials with higher strength. The material's strength can be represented by strain energy density [13]:

$$U = \int_{0}^{\sigma_{\max}} \varepsilon \, d\sigma \tag{1}$$

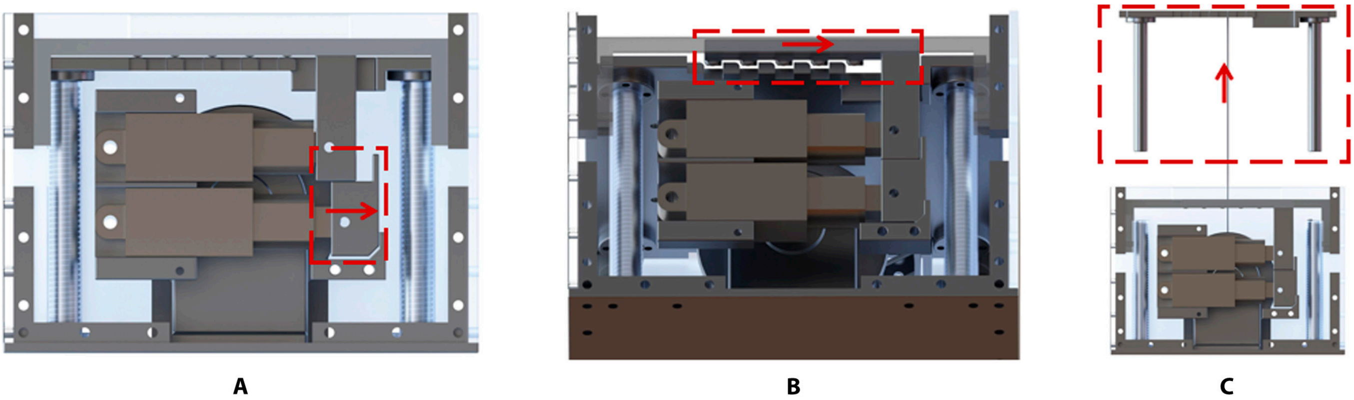

Fig. 2. Workflow schematic diagram of the deployment mechanism. (A) Step 1: Safety unlocking. (B) Step 2: Pusher translation. (C) Step 3: Ejection and deployment.

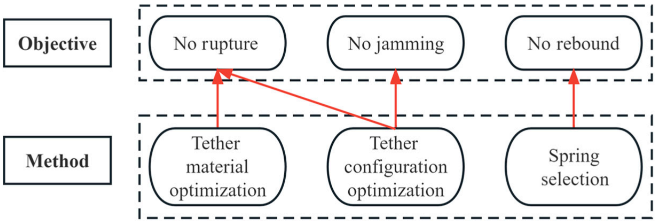

Fig. 3. Content of the "Optimization Method for Electrodynamic Tether Deployment Mechanism" section.

where σ is stress, ε is strain, and $\sigma_{\max}$ is fracture stress. However, due to the difficulty in obtaining the $\sigma - \varepsilon$ curve for actual materials, this subsection defines a virtual strain energy density to replace U:

$$\tilde{U} = \frac{1}{2}\sigma_{\max}\varepsilon_{\max} \tag{2}$$

where $\varepsilon_{\max}$ is fracture strain. Since the modulus of plastic deformation of metals is much smaller than the modulus of elasticity, $\tilde{U}$ must be smaller than U.

Considering that the primary function of the electrodynamic tether is to generate a stable current, the material optimization should also consider electrical conductivity, which can be represented by resistivity ρ.

Taking into account previous orbital experiments and material cost issues, aluminum and its alloys will be the choice for the tether material. Considering that alloys have lower electrical conductivity but higher strength compared to pure aluminum, an electrical conductivity threshold is set to screen materials:

$$\rho < h\rho_{Al}, \tag{3}$$

where ρ_{Al} is the resistivity of pure aluminum. Combining the electrical conductivity and strength criteria, materials can be comprehensively evaluated by a new performance index:

$$I_m = \frac{\tilde{U}}{\rho}. \tag{4}$$

The material with the highest I_m value will be selected as the tether material.

Taking the resistivity threshold $h = 1.4$, the materials in Table 1 can be selected, with the highest I_m value being the 6063-O material. Therefore, the material selected for the electrodynamic tether in this study is 6063-O, which can achieve a comprehensive optimization of conductivity and strength performance.

Table 1. Parameters of selected materials

Materials	$\rho(10^{-8}\Omega\text{m})$	$\sigma_{\max}$(MPa)	$\varepsilon_{\max}$(%)	$\tilde{U}$(MPa)	I_m
Pure aluminum (soft state)	2.8	90	20	9	3.2
Pure aluminum (hard state)	2.9	160	6	4.8	1.7
2014-O	3.4	220	12	13.2	3.9
2017-O	3.5	215	12	12.9	3.7
3003-O	3.5	120	15	9	2.6
3105-O	3.8	130	14	9.1	2.4
5005-O	3.3	120	15	9	2.7
5050-O	3.4	150	16	12	3.5
6061-O	3.7	150	14	10.5	2.8
6063-O	3	130	20	13	4.3
6063-T6	3.3	190	8	7.6	2.3

Optimization to reduce the risk of jamming

Configuration optimization of the main part of tether

To reduce the risk of jamming during the tether deployment, ejection resistance needs to be decrease through tether configuration optimization. However, the strength of the tether with less resistance is generally lower. Therefore, the ratio of ejection resistance to strength can be used as a material evaluation criterion.

When the material is fixed, tensile strength is solely determined by the tether's cross-sectional area S. Thus, the resistance coefficient can be defined to comprehensively evaluate the tensile strength and resistance of the configuration:

$$I_f = \frac{f_{avg}}{S}, \tag{5}$$

where f_{avg} represents average resistance. A smaller I_f indicates better configuration performance.

The resistance measurement method is to stretch the tether vertically using a robot arm. This is performed by fixing the end of the robot arm to a tension sensor and the other end of the tension sensor to the tether. Because the pull is uniform, the tension can be approximated as equal to the resistance.

The results of 6063-O aluminum tethers with different configuration resistance measurements are shown in Table 2. Due to the fact that the minimum tether diameter encountered in orbital experiments and literature is 0.45 mm [11], and tethers with a diameter above 0.7 mm are not feasible as the optimal solution based on measurement data, Table 2 includes only a subset of measurement data.

Based on the data in Table 2, it is evident that the optimal solution combining both strength and resistance can be achieved by using 2 aluminum tethers with a diameter of 0.45 mm for the tether. The state of the tethers wrapped around the reel is illustrated in Fig. 4.

Strength analysis and front-end configuration optimization

In this subsection, an analysis of possible breakage scenarios is conducted. The analysis results indicate that in order to prevent the tethers from rupture due to jamming, it is necessary to make long tether in a relaxed state in front, which cannot be achieved in engineering. To address this issue, a front-end bulking optimization method for the tether configuration is proposed, enabling the tether to deploy with less resistance while avoiding rupture caused by jamming.

To prevent the tether from rupture during the ejection process, it is necessary to ensure that the ultimate virtual strain energy $\tilde{E}$, which represents the maximum energy that the material can absorb, is greater than the end kinetic energy E_k when the tether is released for any length l. Therefore, Eq. 6 can be used as a criterion for the material rupture.

$$\tilde{E} < E_k \tag{6}$$

Referring to Table 1, $\tilde{E}$can be calculated by

$$\tilde{E} = n\pi r^2 l \tilde{U}, \tag{7}$$

where n represents the num of the tether and r represents the radius of the tether. The E_k needs to be obtained through tether deployment simulation.

Table 2. Tensile resistance of different 6063-O aluminum tethers

Tether diameter(mm)	Number of tethers	f_{avg}(N)	l_f(N/mm^2)
0.45	1	0.025	0.157
0.45	2	0.045	0.141
0.5	1	0.035	0.178
0.5	2	0.065	0.166
0.6	1	0.080	0.301
0.6	2	0.145	0.256
0.7	1	0.150	0.390
0.7	2	0.270	0.351

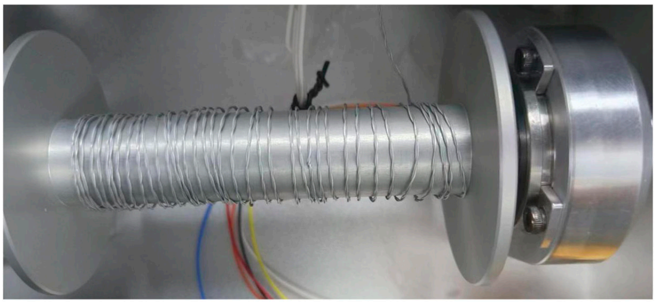

Fig. 4. Two 0.45-mm aluminum tethers wrapped around the reel.

A simplified kinetic model of the tether deployment process is given by Eq. 8 [14]:

$$\begin{gathered}\theta'' + 2\left(\frac{l'}{l} - \phi'\tan\phi\right)\left(\theta' + 1\right) + 3\sin\theta\cos\theta = 0\\ \phi'' + 2\frac{l'}{l}\phi' + \sin\phi\cos\phi\left[\left(\theta' + 1\right)^2 + 3\cos^2\theta\right] = 0\\ l'' - l\left[\phi'^2 + \cos^2\phi\left(\theta' + 1\right)^2 + \left(3\cos^2\theta\cos^2\phi - 1\right)\right] = \frac{Q_L}{m^*\omega_0^2 l l_{\max}},\end{gathered} \tag{8}$$

where θ and ϕ are the in-plane and out-of-plane angles. $l_{\max}$ is the target tether deployment length index. The approximate mass is:

$$m^* = \frac{(m_1 + m_2)(m_2 + m_t/2)}{m_1 + m_2 + m_t} - \frac{m_t}{6}, \tag{9}$$

where m_1 and m_2 refer to the masses of the objects at the respective ends of the tether. ω_0 is the initial attitude angular velocity with respect to the center of mass of the system. Q_L represents the sum of the forces along the tether direction, which can be approximately replaced byf_{avg}.

The optimal initial ejection velocity $v_{0\exp}$ is defined as when the ejection velocity $v$decreases to zero, l just exceeds $l_{\max}$. When ejecting at $v_{0\exp}$, the rebound will not occur by ensuring that the length of tether carried by the mechanism is slightly greater than the $l_{\max}$. The ejection cases corresponding to different $v_{0\exp}$ are basically the same; thus, only the parameters in Table 3 are used as examples, where m_2, tether linear density, and f_{avg} are consistent with the actual situation.

The l and v during the tether deployment vary with time as shown in Fig. 5. It can be seen that when $v_0 = 2.0$ m/s, l cannot reach 50 m; when $v_0 = 2.2$ m/s, a sudden stop occurred in the velocity of the tether, resulting in a rebound phenomenon. However, at an ejection initial velocity of 2.1 m/s, the tether reached a length of 50.3 m, precisely reducing its velocity to zero, which satisfies the definition of $v_{0\exp}$. The precision of $v_{0\exp}$ is 0.1 m/s, as more precise initial velocity is challenging to meet through spring selection.

Table 3. Initial parameter table of ejection deployment simulation

Parameter name	Parameter value	Parameter name	Parameter value
Orbital altitude	600 km	$l_{\max}$	55 m
m_1	4,343 kg	m_2	1 kg
Tether linear density μ	0.68 g/m	f_{avg}	0.045 N
Initial θ	0°	Initial $\dot{\theta}$	0°/s
Initial ϕ	0°	Initial $\dot{\phi}$	0°/s

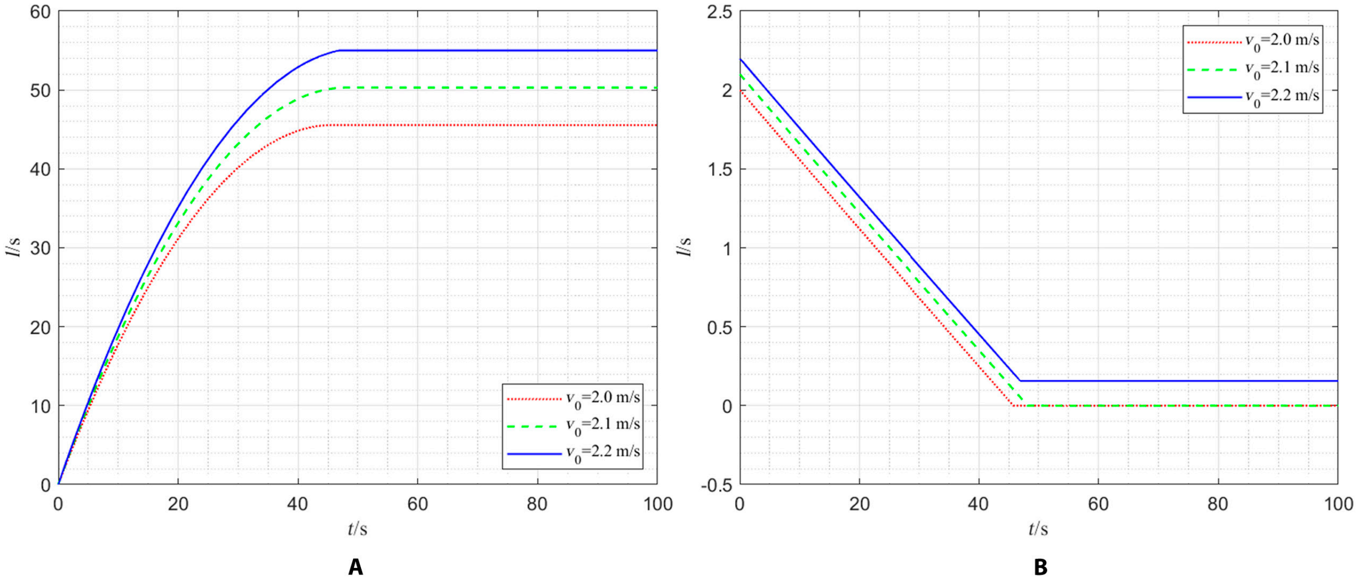

Fig. 5. (A) *l* versus time curve; (B) *v* versus time curve.

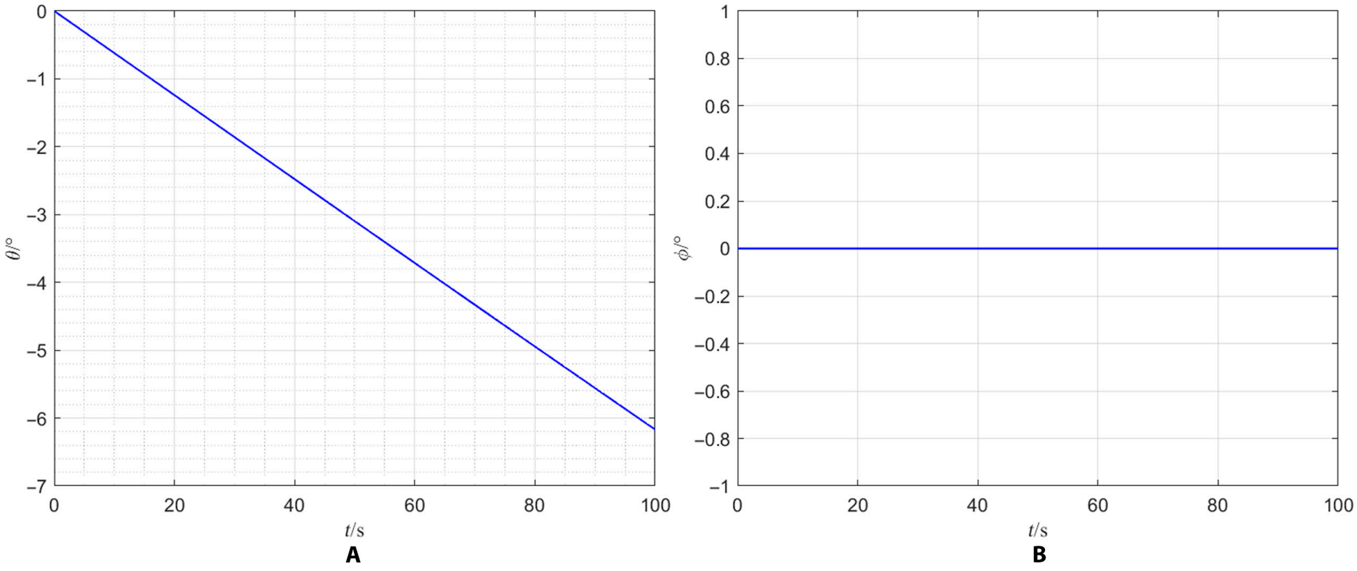

Fig. 6. (A) θ versus time curve; (B) ϕ versus time curve.

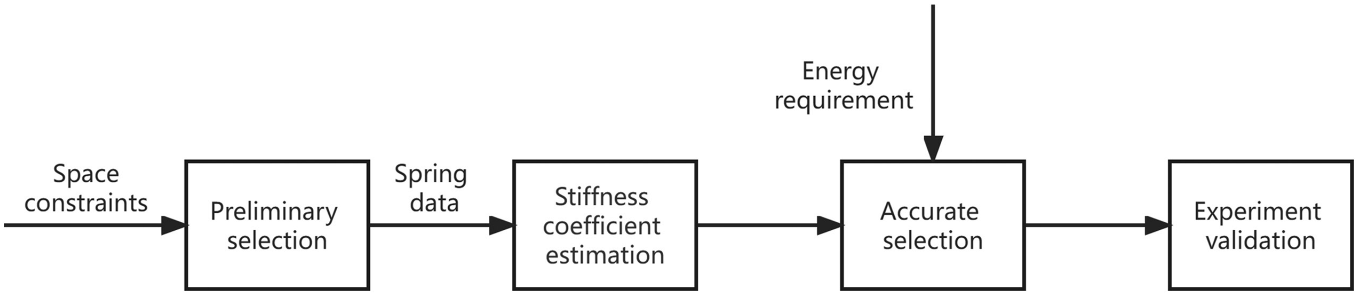

Fig. 7. Spring selection method.

When ejecting at $v_{0\exp}$, the variation process of θ and ϕ of the tether is depicted in Fig. 6. It can be seen that during the whole deployment process, ϕ is always stable at the initial value, while θ decreases continuously from the initial 0° to −3° in 48 s. Owing to the short ejection distance, the fluctuation of θ is small and can be returned to steady state by subsequent current control, but if the uncontrolled ejection distance is too long, instability may occur.

Referring to the results in Fig. 5, it can be seen that the tether deployment at $v_{0\exp}$ can be regarded as a uniformly decelerating linear motion. According to the principles of uniformly decelerating linear motion, v satisfies Eq. 10.

$$v = v_0\sqrt{1-\frac{l}{l_{\max}}} \tag{10}$$

Then, E_k can be calculated using Eq. 11.

$$E_k = \frac{1}{2}m_2v^2 = \frac{1}{2}\left(1-\frac{l}{l_{\max}}\right)m_2v_0^2. \tag{11}$$

Substituting Eqs. 7 and 11 into Eq. 6, the rupture criterion can be obtained as follows:

$$l < \frac{2m_2 l_{\max} v_0^2}{n\pi l_{\max} r^2 \tilde{U} + 2m_2v_0^2} \triangleq l_{stuck}, \tag{12}$$

where l_{stuck} refers to the minimum length of the tether that needs to be released to ensure no rupture occurs. If $l \geq l_{stuck}$, rupture will not occur. To ensure that the tether does not break during the ejection process, a suspended tether with a length of $l_h \geq l_{stuck}$ needs to be placed inside the device. Suspended tether refers to a tether wound inside the device with a curvature much smaller than that of the reel. Due to the fact that the suspended tether does not wrap around the reel, it can be considered that the suspended tether will not cause jamming. In addition, according to the resistance measurement results, the tensile resistance of the suspended tether is approximately 50% of that of the wrapped tether.

The experimental results indicate that when the suspended tether exceeds 3 turns, i.e., a length greater than $l_{upp} = 3\pi D = 1.32$m, jamming may occur due to winding, where $D = 0.14$m is the radius of the inscribed circle on the bottom surface of the mechanism. According to Eq. 12, Table 2, Table 3, and the method to obtain $v_{0\exp}$, it can be calculated that $l_{stuck} = 2.05$ m for the tether selected in the "Configuration optimization of the main part of tether" section, which does not meet the requirements.

To prevent the main tether from breaking due to jamming before releasing 2.05 m, the first 2.05 m of the tether is thickened. The thickened tether may have 2 states: suspended and wrapped. Therefore, to ensure that the defined domain contains all optimal solutions, the tether can be divided into 3 sections. The first section is a thickened suspended tether; the second section is a thickened wrapped tether; the third section is the main tether. To determine the optimal configuration of the tether, the tether selection problem is formulated as the following optimization problem:

$$\begin{aligned} min\ \ \tilde{E}_f &= f_1(n_1,r_1)l_1 + f_2(n_2,r_2)l_2 + f_3(n_3,r_3)l_3 \\ s.t. \quad & l_1 \leq 3\pi D \\ & l_{\max} = l_1 + l_2 + l_3 \\ & f_1(n,r) = 0.5f_2(n,r) \\ & f_2l_2 + f_3l_3 \leq \frac{1}{4}\pi d_1^2 n_1 l_1 \tilde{U} \\ & f_3l_3 \leq \frac{1}{4}\pi d_2^2(n_1l_1 + n_2l_2)\tilde{U} \end{aligned} \tag{13}$$

where n_i, r_i, l_i, $f_i(i=1,2,3)$ represent the num, radius, length, and resistance of the ith section of the tether. The values of n_i, r_i satisfy Eq. 14:

$$\begin{aligned} n_1 &= 2 \\ r_1 &= 0.45\,\text{mm} \\ r_2, r_3 &\in [0.45\,\text{mm}, 0.5\,\text{mm}, 0.6\,\text{mm}, 0.7\,\text{mm}] \\ n_2, n_3 &\in [1, 2] \end{aligned} \tag{14}$$

The objective function of the optimization is the minimum total energy consumption. The last 2 constraints in Eq. 13 represent the idea that after releasing the first and second section of tether, no rupture occurs.

Using the interior point method, it can be concluded that when $l_1 = 0.31$m , $l_2 = 0$m , $d_1 = 0.6$ mm , $n_1 = 2$, the minimum energy consumption of 2.27 J can be achieved while no rupture can be guaranteed during the ejection process.

Optimization to avoid rebound

In order to ensure that there is no rebound during the deployment process, it is necessary to select an appropriate initial velocity and eject at this velocity. The selection of the initial velocity has been completed in the "Strength analysis and front-end configuration optimization" section, and the realization of this velocity needs to be achieved through spring selection. The selection methodology is illustrated in Fig. 7.

1. Step 1: Initial Selection. Firstly, identify the type and material of the spring. Then, based on the space constraints, choose springs that can fit within the mechanism. Finally, using the compression characteristics of the springs, narrow down the selection to an initial range. Input spring data from standard spring within this range into the next step.

According to the task type, the spring type is compression spring, and the material selected is piano steel, known for its favorable mechanical properties. The space constraints of the mechanism dictate that the original length $l_0 > 80$ mm, the compressed length $l_{\min} < 80$ mm, and the outer diameter 8 mm $< D_x <$ 15 mm. According to the manufacturer's data, the linear range of the spring that meets the aforementioned requirements is about 20%, so $l_0 \leq 100$ mm. Based on the above constraints, standard springs are selected as shown in the Appendix.

2. Step 2: Stiffness Coefficient Estimation. Within the linear range, the energy storageE_x of a spring is solely determined by its stiffness coefficient K_x and compression amount Δx, which means:

Appendix.

Index	Model name	Dx/mm	L0/mm	Ds/mm	Kx/(N/mm)
1	LHL 375B 7A	8.33	101.6	1.47	4.203
2	LHL 375A 7A	8.81	101.6	1.32	2.452
3	LHL 375D 7A	9.02	101.6	1.8	9.019
4	LHL 375C 7A	9.02	101.6	1.7	6.655
5	LC 047E 22 M	9.14	88.9	1.19	1.646
6	LC 049E 21 M	9.14	88.9	1.24	1.909
7	LC 051E 21 M	9.14	88.9	1.3	2.207
8	LC 055E 21 M	9.14	88.9	1.4	2.995
9	LC 059E 21 M	9.14	88.9	1.5	3.818
10	LC 047E 21 M	9.14	82.55	1.19	1.769
11	LC 049E 20 M	9.14	82.55	1.24	2.067
12	LC 051E 20 M	9.14	82.55	1.3	2.382
13	LC 055E 20 M	9.14	82.55	1.4	3.24
14	LC 059E 20 M	9.14	82.55	1.5	4.151
15	LCM160FG 05 M	11.6	85	1.6	3.664
16	LCD160FG 05 M	11.6	85	1.6	3.609
17	LHL 500B 08	11.71	88.9	2.03	8.231
18	LHL 500B 8A	11.71	101.6	2.03	7.531
19	LHL 500A 08	11.84	88.9	1.83	5.254
20	LHL 500AB 08	12.07	88.9	1.98	6.655
21	LHL 500A 8A	12.07	101.6	1.83	4.816
22	LHL 500C 08	12.12	88.9	2.21	11.209
23	LHL 500C 8A	12.12	101.6	2.21	10.508
24	LHL 500A 09	12.14	114.3	1.91	4.378
25	LHL 500D 08	12.19	88.9	2.34	14.011
26	LC 072G 15 M	12.19	88.9	1.83	4.641
27	LC 075G 15	12.19	88.9	1.91	5.324
28	LC 072GG 15M	12.7	88.9	1.83	3.722
29	LC 072GG 14M	12.7	82.55	1.83	4.022
30	LC 091GJ 13M	14.3	88.9	2.31	9.296
31	LC 054GJ 13M	14.3	88.9	1.37	0.859
32	LC 091GJ 15M	14.3	101.6	2.31	8.079
33	LC 054GJ 15M	14.3	101.6	1.37	0.748
34	LC 091GJ 12M	14.3	82.55	2.31	10.054
35	LC 054GJ 12M	14.3	82.55	1.37	0.927
36	LC 091GJ 14M	14.3	95.25	2.31	8.645
37	LC 054GJ 14M	14.3	95.25	1.37	0.799
38	LHL 625A 09	14.35	101.6	2.29	7.706
39	LCM200GM 05 M	14.5	105	2	4.58
40	LCD200GM 05 M	14.5	105	2	4.521
41	LHL 625A 08	14.61	88.9	2.29	8.406
42	LHL 625AB 08	14.73	88.9	2.49	11.734
43	LHL 625AB 09	14.73	101.6	2.49	10.508
44	LHL 625B 09	14.78	101.6	2.67	13.31
45	LHL 625B 08	14.88	88.9	2.67	14.886
46	LHL 625C 08	14.99	88.9	2.84	21.366

$$E_x = \frac{1}{2} K_x \Delta x^2. \tag{15}$$

Δx can be calculated based on the difference between l_0 and the device dimensions, while the K_x data can only be obtained from standard spring tables. Due to the inconsistency between commercial spring and standard spring models, for precise selection of commercial springs, it is necessary to estimate K_x of any spring model based on the data from standard springs.

$$K_x = G \frac{d_x^4}{n D_m^3}, \tag{16}$$

where G is an unknown parameter, d_x is the tether diameter, n is the effective number of turns, and $D_m = D_x - d_x$ is the mean diameter. Since commercial spring models only contain D_x, d_x, l_0, the $n = c\frac{l_0}{d_x}$ and $G^{'} = cG$ approximations are performed to get:

$$K_x = G^{'} \frac{d_x^5}{l_0 \left(D_x - d_x\right)^3} \tag{17}$$

Calculate and draw a $K_x - \frac{10^5 d_x^5}{l_0 (D_x - d_x)^3}$ scatter plot based on the data from the Appendix, as shown in Fig. 8:

Using the least squares method for fitting, the slope can be considered as an estimate of $G^{'}$, i.e., $\tilde{G}^{'} = 3.2758$. The correlation coefficient $R^2 = 0.99175$ demonstrates the effectiveness of the fit. The final approximate formula for K_x is:

$$\tilde{K}_x = 10^5 \tilde{G}' \frac{d_x^5}{l_0 \left(D_x - d_x\right)^3} \tag{18}$$

3. Step 3: Accurate Selection. According to Eq. 18 and Hooke's law, the energy storage capacity of any spring within the selected range can be estimated using Eq. 12.

$$\tilde{E}_x = \frac{1}{2} 10^5 \tilde{G}' \frac{d_x^5}{l_0 \left(D_x - d_x\right)^3} \left(l_0 - l_m\right)^2, \tag{19}$$

where $\tilde{E}_x$ represents the theoretical energy storage of the spring and l_m is the actual compression length. Considering the energy loss rate, it is advisable to choose a spring with a $\tilde{E}_x$ value slightly greater than the energy criterion E_r as the precise selection result. Therefore, the selection criterion is

$$\tilde{E}_x = (1 + \varepsilon) E_r. \tag{20}$$

In this paper, with the values of $\varepsilon = 0.15$, $l_m = 90\,\mathrm{mm}$, and $E_r = \frac{2.27}{4} = 0.5675\,\mathrm{J}$ chosen as mentioned, the optimal spring selection can be obtained as $D_x = 13\,\mathrm{mm}$, $d_x = 1.4\,\mathrm{mm}$, $l_0 = 90\,\mathrm{mm}$, and $\tilde{E}_x = 0.6271\,\mathrm{J} = 1.11 E_r$.

4. Step 4: Experimental Verification. Use the selected spring for ejection and calculate the initial kinetic energy E_{k0}. If E_{k0} is slightly greater than $4E_r$, it is considered that the spring has the capability to fully deploy the tether. Due to the difficulty of simulating the deployment of a long-distance tether in ground experiments, this paper focuses on verifying E_{k0}.

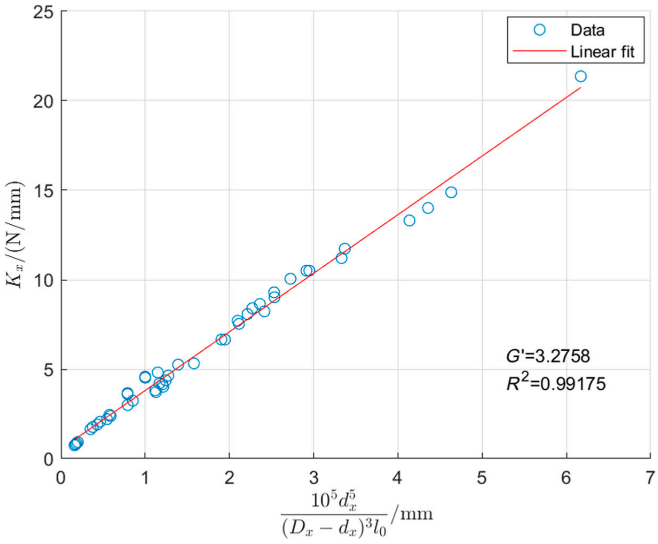

Fig. 8.

The mechanism used for ejection is shown in Fig. 9. A part of the shell of the mechanism in Fig. 9 has been removed to show the internal structure more clearly.

The experimental process used the ground oblique throw ejection experiment. Let the angle of the oblique throw be θ, the height of the starting point of the oblique throw be h, the initial velocity of the oblique throw be v_0, and the horizontal projection distance from the starting point of the oblique throw be L. According to the law of oblique throwing motion [15], E_{k0} can be solved as

$$E_{k0} = \frac{1}{2} m \frac{L^2}{cos^2\theta} \frac{g}{2(L\,tan\,\theta + h)}. \tag{21}$$

In the actual experiment, $m = 1\,\text{kg}, \theta = arcsin\left(\frac{44}{160}\right), L = 0.47\,\text{m}$, $h = 0.12$ m, and $g = 9.8$ m/s^2, so that $E_{k0} = 2.30\,\text{J} > 4E_r$. Therefore, this experiment proves that the selected spring has the ability to eject and deploy a 50-m tether. Moreover, when the carried tether exceeds 50 m, there will be no rebound during the deployment process.

Discussion

To solve the problem of past electrodynamic tether in-track experiments due to the failure of the deployment mechanism, this paper proposes a pusher motor-based electrodynamic tether deployment mechanism with a size of 2 U and a weight 2.3 kg. Compared with the existing mechanism, it has certain advantages in terms of safety, synchronization, experimental cost, size, and weight. At the same time, the selection and optimization of the tether and spring are carried out to ensure that the mechanism can deploy the tether smoothly, without jamming or rupture. In the ground experiment, the top plate was ejected with a kinetic energy of 2.3 J, which is capable of deploying a tether of at least 50 m, and the tether successfully unfolded. The results indicate the effectiveness of the optimization algorithm.

In the future, space-grade environmental tests will be performed on the designed mechanism. Additionally, the tether capacity of the device will be improved up to at least 1 km for practical deorbit task [16].

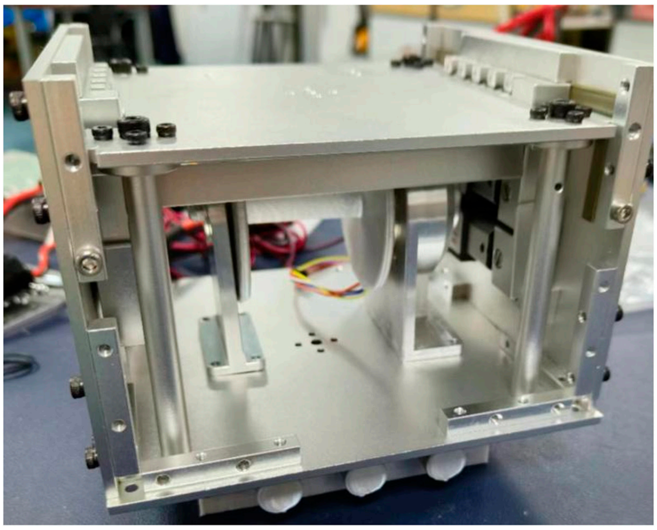

Fig. 9. Physical diagram of the mechanism.

Acknowledgments

Funding: This work was supported by the State Administration of Science, Technology and Industry for National Defense KJSP202360201.
Author contributions: J.Z. conceived the idea for this review and supervised the study. Y.Y. wrote the manuscript. K.Y. and C.Z. revised the manuscript. H.C. and L.L. examined and corrected the problems with the language. All the authors discussed the results and contributed to the final version of the manuscript.
Competing interests: The authors declare that they have no competing interests.

Data Availability

The data of this study are available from the corresponding author upon request.

References

1. Valmorbida A, Olivieri L, Brunello A, Sarego G, Sánchez-Arriaga LEC, Lorenzini EC. Validation of enabling technologies for deorbiting devices based on electrodynamic tethers. *Acta Astronaut*. 2022;198:707–719.
2. Zhang J, Xiao Q, Li L. Solution space exploration of low-thrust minimum-time trajectory optimization by combining two homotopies. *Automatica*. 2023;148:110798.
3. Zhang J, Li X, Yang K, Li Y. A high-fidelity high-efficiency model for electrodynamic tether system based on recursive algorithm. *Acta Astronaut*. 2022;198:617–630.
4. Zhang J, Zhang R, Yang K. Attitude stability analysis and configuration design of pyramid drag sail for deorbit missions. *J Aerosp Eng*. 2022;35(6):04022084.
5. Yasushi O, Kawamoto S, Okumura T, Iki K, Okamoto H, Inoue K, Uchiyama T, Tsujita D. Review of KITE—Electrodynamic tether experiment on the H-II transfer vehicle. *Acta Astronaut*. 2020;177:750–758.
6. Zhu Z, Zhong R. Deorbiting dynamics of electrodynamic tether. *Intl J Aerospace Lightweight Struct*. 2011;1(1):S2010428611000043.

7. Liu J, Li G, Zhu Z, Zhan X. Orbital boost characteristics of spacecraft by electrodynamic tethers with consideration of electric-magnetic-dynamic energy coupling. *Acta Astronaut*. 2020;171:196–207.
8. Dobrowolny M, Stone NH. A technical overview of TSS-1: The first tethered-satellite system mission. *Il Nuovo Cimento C*. 1994;17:1–12.
9. Irastorza IG, Aznar F, Castel J. Gaseous time projection chambers for rare event detection: Results from the T-REX project. II. Dark matter. *JCAP*. 2016;2016(01):46–53.
10. Zhong Z, Zhang H, Zhou J, Huang Y. Review of non-pyrotechnic connection and separation technology of spacecraft. *Manned Spaceflight*. 2019;25(01):128–142.
11. Yamagiwa Y, Nohmi M, Aoki Y, Momonoi Y, Nanba H, Aiga M, Kumao T, Watahiki M. Space experiments on basic technologies for a space elevator using microsatellites. *Acta Astronautica*. 2017;138:570–578.
12. Wu Z, Chen Y, Xu W. A light space manipulator with high load-to-weight ratio: System development and compliance control. *Space: Sci Technol*. 2021;2021:9760520.
13. Sih GC, Macdonald B. Fracture mechanics applied to engineering problems-strain energy density fracture criterion. *Eng Fract Mech*. 1974;6(2):361–386.
14. Xiao H. *Deployment and position control of electrodynamic tether*. Harbin: Harbin Institute of Technology; 2020.
15. Liu J, Liu J. Newton's laws of motion. *Lect Notes Theor Mec*. 2019;99–102.
16. Vannaroni G, Dobrowolny M, Venuto DF. Deorbiting with electrodynamic tethers: Comparison between different tether configurations. *Space Debris*. 1999;1:159–172.